Journal of
Materials Chemistry A

PAPER

View Article Online
View Journal | View Issue

Cite this: *J. Mater. Chem. A*, 2024, **12**, 18324

Biomass-derived B/N/P co-doped porous carbons as bifunctional materials for supercapacitors and sodium-ion batteries†

Yanjiao Li,[a] Xufei Zou,[a] Shiqi Li,[a] Yingying Chen,*[ab] Guoxiu Wang,[b]
Hongxun Yang*[a] and Hao Tian*[b]

Porous carbon materials as one of the most promising electrodes for energy storage and conversion devices have attracted considerable attention because of their large specific surface area, well-developed pore structure, excellent electrical conductivity and low cost. However, the traditional production of porous carbon is often accompanied by complex synthesis conditions, environmental pollution and large energy consumption. Herein, a new type of B/N/P co-doped porous carbon (OPBNP) was prepared using a simple hydrothermal doping method combined with a low-temperature carbonization–activation process using orange peel (OP) as the precursor, and boric acid and diammonium phosphate as co-dopant. The carefully regulated elemental doping and low carbonization temperature (600 °C) endow the prepared OPBNP material with a high specific surface area (1774.8 m^2 g^{-1}), microporous-dominated hierarchical structure, larger graphite interlayer spacing (0.392 nm), and more defects. The combination of structurally strategic design and multi-atom doping promotes fast charging and long-lasting stability. As electrodes in supercapacitors (SCs), the OPBNP delivers a superior specific capacitance of 289 F g^{-1} at 5 A g^{-1} with 93.6% capacitance retention after 10 000 cycles. Besides, the assembled OPBNP//OPBNP symmetric supercapacitor could reach a high energy density of 8.9 W h kg^{-1} at a power density of 499.7 W kg^{-1}. Furthermore, as anodes for sodium ion batteries (SIBs), OPBNP exhibits a high reversible capacity of 292.3 mA h g^{-1} after 100 cycles at 0.1 A g^{-1} and an excellent cycling performance of 206.6 mA h g^{-1} after 1000 cycles at 1 A g^{-1}. The B/N/P co-doped porous carbon has the characteristics of low cost, simple preparation and excellent properties, making it a great potential electrode for advanced supercapacitors and sodium ion batteries.

Received 30th March 2024
Accepted 17th June 2024

DOI: 10.1039/d4ta02115k

rsc.li/materials-a

1. Introduction

Supercapacitors (SCs) and sodium-ion batteries (SIBs) have become the most promising energy storage conversion devices today. They have the potential to significantly alleviate the lithium resource scarcity inherent in traditional lithium-ion batteries (LIBs) and demonstrate promising market prospects.[1–3] Developing electrode materials with low cost and high performance is the crux of improving the performance of energy storage and conversion devices (SCs and SIBs).[4–6] Porous carbon materials have been extensively studied owing to their large specific surface area (SSA), enriched pore structure, excellent electrical conductivity and low cost.[7–10] However, the traditional production of porous carbon is often accompanied by complex synthesis conditions, serious environmental pollution and large energy consumption. As a renewable green raw material, biomass is considered a very promising precursor for manufacturing functional carbon because of its rich resources, helping to achieve sustainable energy utilization and environmental protection, low cost, *etc.* In particular, biomass-based carbon such as rice husk,[11] wheat-straw,[12] bagasse,[13] pomelo peels,[14] and waste palm[15] have unique structural properties as bioresidual materials. Besides, their inherent hierarchical porous structure can provide a large accessible surface area and smooth transfer paths for electrolyte ions. Furthermore, most of the biomass materials contain the elements of N, S, and P. Thus, heteroatom self-doping can be achieved in the synthesis of materials to form additional active sites in the biomass-based carbon materials. Therefore, the development of high-performance porous carbon-based materials with controlled pore structure and composition using biomass as a precursor can not only save cost and alleviate environmental pollution but also achieve the high-value utilization of biomass.

---

[a] *School of Environmental and Chemical Engineering, Jiangsu University of Science and Technology, Zhenjiang 212003, Jiangsu, China. E-mail: scyyh@just.edu.cn; yhongxun@126.com*

[b] *Centre for Clean Energy Technology, School of Mathematical and Physical Sciences, Faculty of Science, University of Technology Sydney, Broadway, NSW 2007, Australia. E-mail: hao.tian@uts.edu.au*

† Electronic supplementary information (ESI) available. See DOI: **https://doi.org/10.1039/d4ta02115k**

Activation conditions and heteroatom doping also show significant effects on the pore structure and surface chemistry of porous carbon.[16,17] Traditional porous carbon material is usually obtained by one-step or two-step high-temperature pyrolysis (usually above 700 °C) combined with activation, resulting in a high energy consumption.[9,18] In recent years, hydrothermal carbonization technology (HCT) has been used for waste biomass treatment due to its low energy consumption and high efficiency.[19–22] At relatively mild temperatures (180–250 °C), waste biomass in the water environment tends to be rich in oxygen-containing functional groups, which have considerable activation potential and can produce porous structures with high porosity. Simultaneously, the hydrothermal method can effectively stabilize heteroatom doping and improve graphitization, thereby improving the capacitance performance of biomass carbon materials.[23] The introduction of other heteroatoms, such as N, P, and B, into carbon materials can not only significantly improve the wettability of carbon materials to the electrolyte and promote the ionic transport rate but also provide more electrochemical active sites to enhance the capacity of the materials, thus effectively improving the energy density and rate capabilities. Wang *et al.* developed N/P/O heteroatom-doped porous activated carbon using durian shells as raw material and $(NH_4)_2HPO_4$ as a doping reagent by applying a hydrothermal method, delivering a high capacitance of 560 F g^{-1} at 2 A g^{-1} and good cycle stability (retention rate of 88% after 10 000 cycles).[24] Tang *et al.* reported B/N/P co-doped cornstalk-based carbon, exhibiting rich porosity structure and showing a good electrochemical performance (a high specific capacitance of 342.5 F g^{-1} at 0.5 A g^{-1}).[25] In addition, Tao and his co-workers prepared N/P co-doping mesoporous hard carbon derived from soybean root exhibiting high electrochemical performance for both SIBs and potassium ion batteries (PIBs), which can be attributed to the fact that N and P elements can effectively increase the interlayer spacing of the hard carbon and provide more active sites.[26] Muruganantham *et al.* confirmed that the reversible capacity of N/S co-doped carbon derived from mango peel is significantly higher than that of the un-doped carbon material.[27] Orange juice is one of the most widely consumed beverages today. Its large-scale production meets people's needs, but it also produces a large amount of waste orange peel (OP).[28,29] OP mainly comprises cellulose, hemicellulose, pectin and lignin, which are known as good carbon precursors. It is reported that OP-derived carbon materials have been employed in catalysis,[30] gas sensors,[31] Pb–C mixed SCs,[32] LIBs/SIBs,[33] PIBs,[34] *etc.* However, most OPs are discarded and burned as waste due to the lack of effective and inexpensive synthesis methods, resulting in environmental pollution and resource waste. Therefore, it is necessary to explore how to prepare a high-performance biomass carbon material from OP through hydrothermal heteroatom doping and low-temperature activation technology. To the best of our knowledge, there is no report on OP-derived B/N/P co-doped porous carbons as electrodes for SCs and SIBs.

Herein, we report a new B/N/P co-doped porous carbon (OPBNP) by employing OP as a carbon source, boric acid and $(NH_4)_2HPO_4$ as a dopant, using hydrothermal heteroatom doping and a low-temperature KOH activation method. The OPBNP exhibits a high SSA of 774.8 m^2 g^{-1}, larger interlayer spacing of 0.392 nm, and rich interpenetrate network porous structure, which could facilitate the transport of ions and electrons in the electrodes. Simultaneously, the synergistic co-doping of the B/N/P atom can greatly promote the physical and chemical properties of carbon and provide additional pseudopocapacitance and high wettability through the occurrence of redox reactions, ensuring high energy density.[35] Used as an anode electrode for SCs and SIBs, the OPBNP exhibited excellent storage performance, high specific capacity and superior rate performances. This work provides a simple and new preparation method for developing heteroatom-doped carbon, which is helpful in further promoting its application in the field of energy storage.

2. Experimental section

2.1 Materials

Orange peels (OPs) were collected from the Zhenjiang fruit market. The orange peels were first rinsed in deionized water to remove impurities, such as fouling, and then vacuum dried at 80 °C overnight. After that, the clean OPs were crushed into fine powder by applying a pulverizer and stored in a clean flask under dry conditions for further use. All chemicals in our research were used directly as received without further purification. Distilled water was used throughout the experiment.

2.2 Synthesis of B/N/P co-doped porous carbon

First, 2 g of OP powder, 1 g of $(NH_4)_2HPO_4$, and 1 g of boric acid were added into 60 ml of deionized water to stir for 4 h to obtain a suspension. Then, the suspension was transferred into a 100 ml stainless steel sealed high-pressure reaction kettle and kept at 180 °C for 12 h. After natural cooling to room temperature and vacuum filtration, the as-obtained samples were collected by washing with deionized water and drying overnight at 80 °C to obtain hydrothermally doping products. Next, the products and KOH were dissolved in 50 ml of deionized water at a mass ratio of 1 : 3 after stirring at room temperature for 10 h and then dried at 100 °C for later use. The obtained products were then tiled in a nickel porcelain boat and placed in a tube furnace for calcination activation for 3 h at 600 °C at a heating rate of 3 °C min^{-1} under a nitrogen atmosphere. The obtained black samples were washed with 2 M HCl to remove the salt residue, then washed with deionized water to neutralize, and dried overnight at 80 °C to obtain the resultant B/N/P co-doped porous carbon (OPBNP). The detailed synthesis process of OPBNP in this study is shown in Scheme 1.

For comparison, the sample prepared using a similar method without the addition of $(NH_4)_2HPO_4$ and boric acid was denoted as OPC. The sample synthesized *via* a similar method with only $(NH_4)_2HPO_4$ was denoted as OPNP, and the sample with only boric acid was denoted as OPB.

2.3 Characterizations

The phase structure and chemical composition of the porous carbon materials were characterized by X-ray diffraction (XRD,

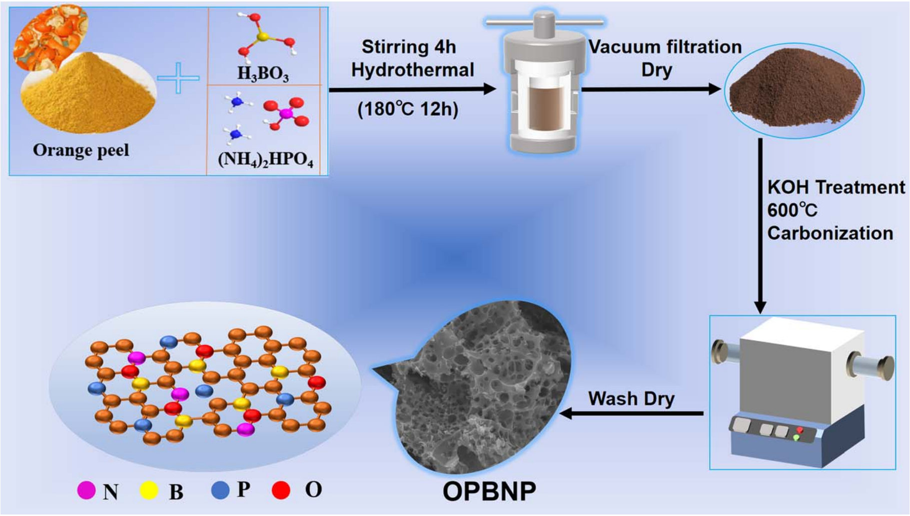

Scheme 1 Schematic diagram of the OPBNP preparation process.

Shimadzu XRD-6000) with Cu Kα radiation ($\lambda = 0.15406$ nm). The morphology was investigated using scanning electron microscopy (SEM, Quanta FEG 250) and high-resolution transmission electron microscopy (HRTEM, Tecnai G2 F20). The specific surface areas, pore volume and pore diameter of carbon materials were analyzed by nitrogen adsorption–desorption measurements (Micrometric, JW-BK200B) and calculated by Brunauer–Emmett–Teller theory and non-local density functional theory methods. The chemical states of the elements were further investigated by X-ray photoelectron spectroscopy (XPS, Thermo Fisher Nexisa). Raman spectra of the as-synthesized sample were carried out using a Renishaw Raman spectrometer.

2.4 Electrochemical measurements of supercapacitors

The electrochemical properties of the samples for supercapacitors were evaluated in both three-electrode half-cells and two-electrode systems within a 6 M KOH electrolyte. Working electrodes were prepared by mixing the active carbonaceous material (80%), the conductive agent acetylene black (10%), and the binder polyvinylidene fluoride (PVDF) (10%) in *N*-methylpyrrolidone (NMP) to produce a uniform thick slurry. Then, the mixed slurry was coated on nickel foams (1×2 cm^2) pretreated with acetone and hydrochloric acid. The electrode materials were then placed in a vacuum drying oven and dried for 12 h at 80 °C, followed by pressing into a film at a pressure of 10 MPa. The loading mass of the active material was 1–2 mg cm^{-2}. The Pt foil and Hg/HgO electrodes were used as the counter and reference electrodes, respectively. Galvanostatic charge–discharge (GCD) and cyclic voltammetry (CV) measurements were conducted in the voltage range of −1–0 V (*vs.* Hg/HgO). Electrochemical impedance spectroscopy (EIS) with a frequency range of 10^5–10^{-2} Hz and an amplitude of 5 mV was conducted on an electrochemical workstation (CHI660E, Shanghai, China). Cycling stability was tested using a battery test instrument (CT2001A, Wuhan Blue Electronics Co., Ltd). The symmetrical supercapacitor devices were assembled using two working electrodes with the same mass of active substances (loading weight of about 2 mg cm^{-2}) in the CR2032 button cell, Whatman glass fiber (GF/D) as the separator, and 6 M KOH as the electrolyte solution. The measurements of full cells were performed in a voltage range of 0–1 V. Detailed specific calculation formulas for electrochemical performance testing are provided in ESI Text S1.†

2.5 Electrochemical measurements of SIBs

For the SIB tests, the electrode materials were assembled into a button half-cell of CR2032 to measure the electrochemical performance. The preparation of working electrodes was the same as that of supercapacitors; the difference was that the slurry was uniformly smeared on the Cu foil current collector. After drying at 70 °C for 12 h in a vacuum drying oven, the electrode pieces were cut into circular plates with a diameter of 12 mm. Under 0.01 ppm, the cells were assembled with metallic Na for both reference and counter electrodes in a glovebox in argon with moisture and oxygen content. A glass microfiber filter (Whatman GF/D) was used as the separator, and sodium perchlorate ($NaClO_4$, 1 M $NaClO_4$ in EC : PC = 1 : 1 vol% with 50% FEC) was used as the electrolyte. The assembled cells were evaluated by galvanostatic discharge–charge using the LAND battery test system. CV measurements were completed on an electrochemical workstation (CHI 760E, Chenhua Instruments Co. Ltd, Shanghai) in the voltage range of 0.01–3.0 V and a scan rate of 0.1–1 mV s^{-1}. The EIS spectra were measured on an Autolab-PGSTAT 302N electrochemical workstation with frequencies ranging from 100 kHz to 10 mHz and an amplitude of 5 mV.

3. Results and discussion

3.1 Structural characterizations

Scheme 1 illustrates the detailed synthesis process of OPBNP in this study. SEM has often been used to study the surface morphology and microstructure of derived carbon materials, which play an important role in electrochemical performance.

Fig. 1a shows the SEM of OPC obtained through direct hydrothermal treatment and subsequent calcination without doping and activation. Using hydrothermal driving, most irregular sheets transform into carbon microspheres characterized by smooth surfaces. There is no evident porous network structure, and the surface is covered with debris particles. Fig. 1b–d shows the SEM of OPB, OPNP and OPBNP obtained by doping and subsequent KOH activation carbonization. All the samples demonstrate dense pore structures, which are attributed to the effects of B/N/P doping and KOH activation. Compared with the three samples, both OPB and OPNP show a broken pore structure, while OPBNP appears more complete with uniform pore distribution. Fig. S1† shows the original morphology of OP before hydrothermal treatment, displaying a rough surface and irregular sheet structure, which is very different from the morphology of activation and calcination after hydrothermal treatment at 180 °C (Fig. 1b–d). This result indicates that multi-atomic doping and activation could affect the surface morphology and microstructure of OP-based carbons. TEM results further confirm these porous structural characteristics, and the results are shown in Fig. 1e–h. The OPC in Fig. 1e clearly shows a carbon microsphere and partly sheet structure, which are consistent with the SEM results depicted in Fig. 1a. After heteroatom doping and KOH activation, many pores emerged among the samples due to the departure of inorganic matter. Besides, as the variety of doping elements expands, the pores become smaller and denser. In particular, the TEM image in Fig. 1h shows the richest pore structure, and numerous tiny holes are connected to form a super three-dimensional porous network. The interpenetrating network structure can not only provide a high surface area to allow for more reaction active sites for higher specific capacitance but also slow down the volume expansion during the charge/discharge process and shorten the transmission distance of electrons and ions, thereby improving energy storage capability.[15,18,23,27] The lattice structure of the porous carbon was further analyzed by high-resolution TEM (HR-TEM), as depicted in Fig. 1i and j. A large number of randomly distributed micro/mesopores were

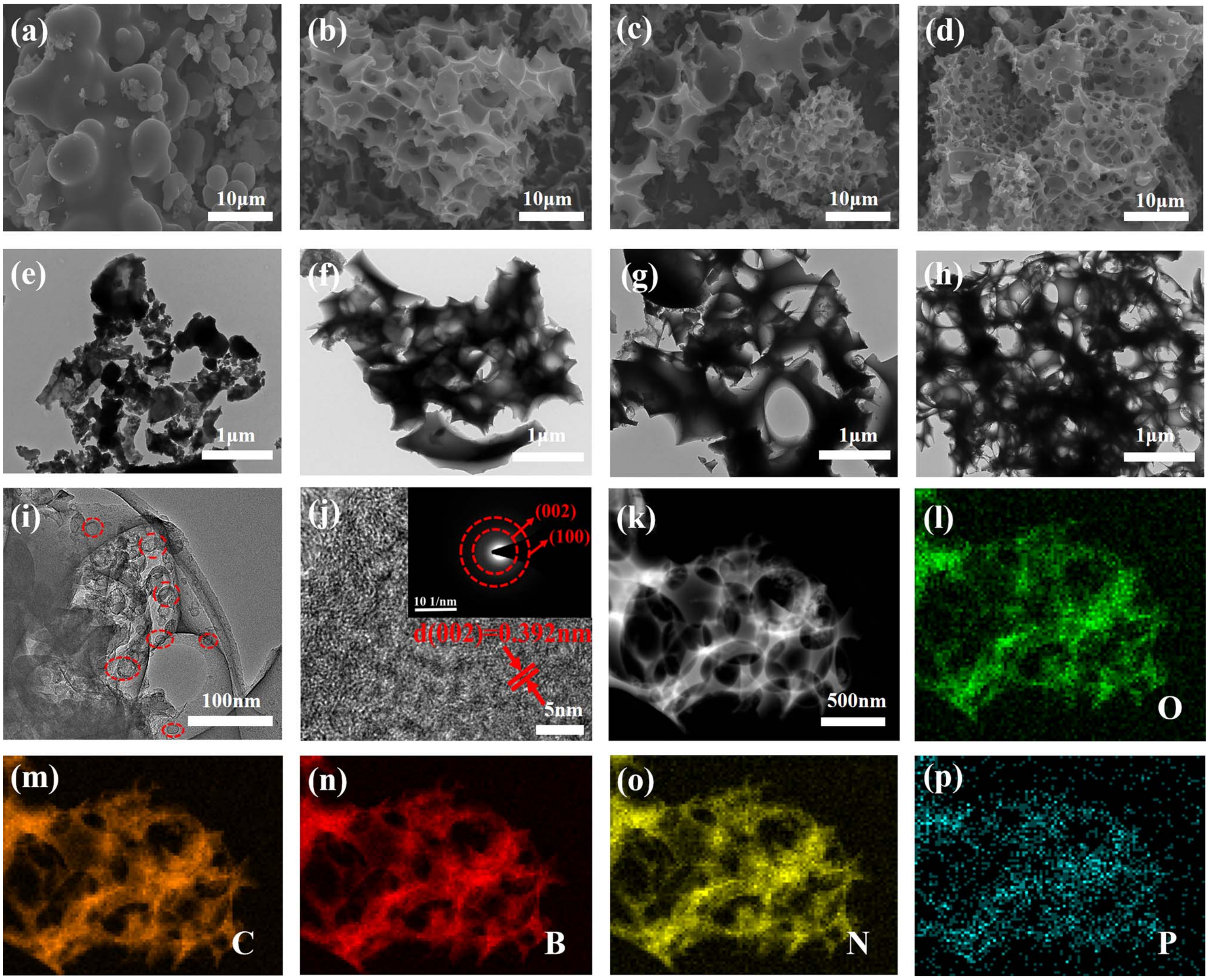

Fig. 1 SEM images of (a) OPC, (b) OPB, (c) OPNP, and (d) OPBNP; TEM images of (e) OPC, (f) OPB, (g) OPNP, and (h) OPBNP; (i) HRTEM; (j) STEM image of OPBNP, (inset): SAED pattern; and (k–p) the corresponding elemental mappings of O, C, B, N, and P.

staggered distribution in carbon nanolayers. Moreover, the carbon nanosheet is mainly amorphous carbon with partially ordered graphite domains, which is beneficial for providing defects or active layers for ion storage.[36] The SAED image illustrated in the inset in Fig. 1j shows a typical diffraction ring of the non-graphite hard carbon structure, indicating that OPBNP is a typical amorphous carbon material.[37] Elemental mapping was used to verify the elemental composition and distribution of the materials. As shown in Fig. 1l–p, OPBNP mainly comprises O, C, B, N and P elements, indicating the successful doping of B, N and P elements.

XRD test was adopted to investigate the crystalline structure and composition of OPC, OPB, OPNP and OPBNP (Fig. 2a). All the samples show a wide diffraction peak near 23° and a weak peak near 43°, corresponding to the (002) plane of amorphous carbon and (100) planes of amorphous character and the graphitic nature, respectively.[33] It is noteworthy that the OPC shows a relatively sharp (002) peak, while OPB, OPNP and OPBNP show a wider peak. In addition, for OPBNP, the (002) crystal plane slightly shifts to a lower diffraction angle due to the doping of B, N, P and KOH activation.[38] The activation and heteroatom doping lead to the formation of defects within the carbon structure, further reducing the graphite degree of the carbon structure and the increase in interlayer distance. The interlayer spacing of the OPBNP is 0.392 nm, which is larger than those of OPC (0.374 nm), OPB (0.378 nm) and OPNP (0.384 nm) (Text S1†). The calculated value is also much greater than the layer spacing of graphite (0.335 nm), which is conducive to

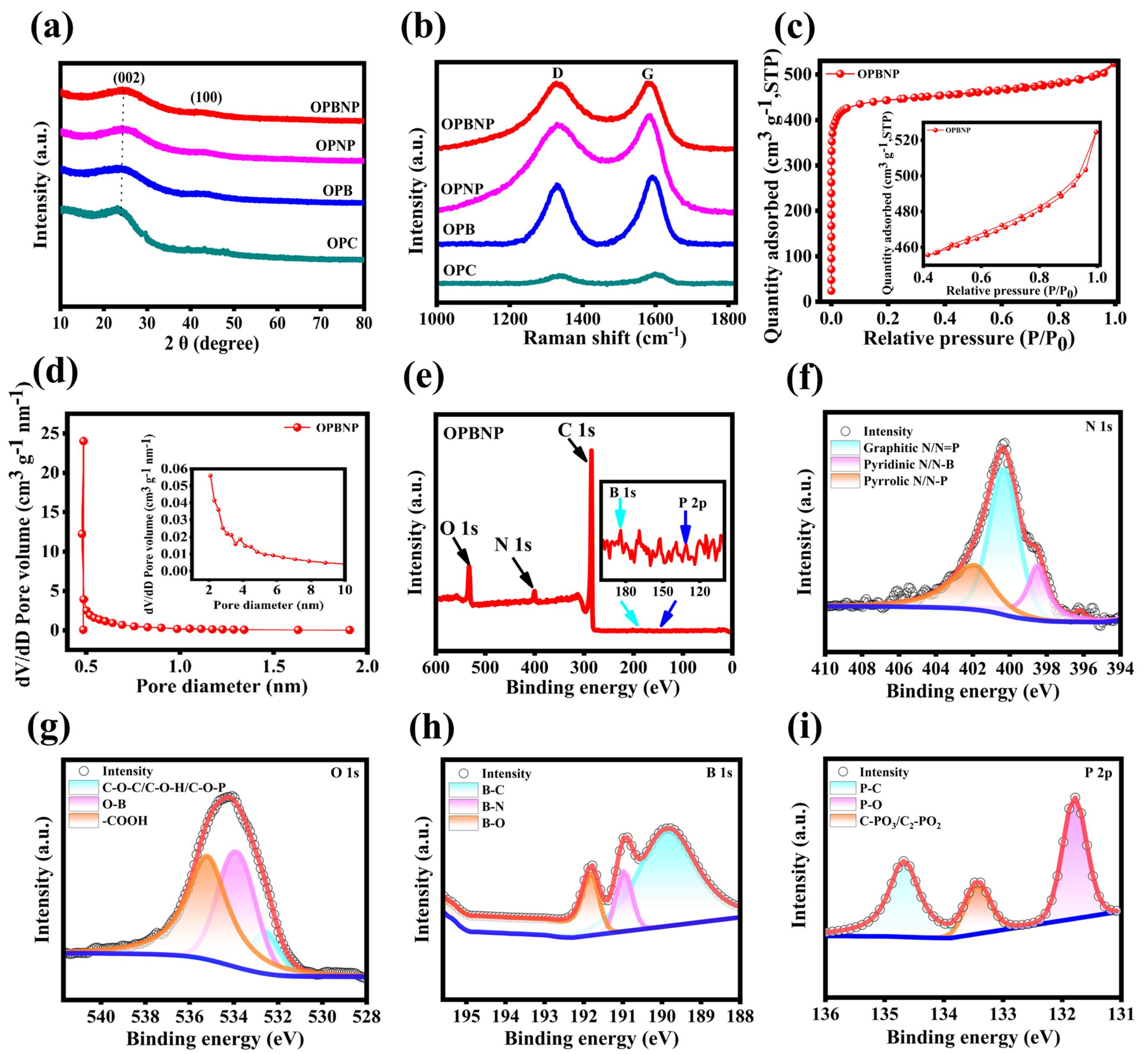

Fig. 2 (a) XRD spectra and (b) Raman spectra of OPC, OPB, OPNP and OPBNP; (c) N_2 adsorption–desorption isotherms and (d) pore size distribution of the OPBNP; (e) XPS survey spectra, inset: B 1s and P 2p amplification region; high-resolution XPS spectra of (f) N 1s, (g) O 1s, (h) B 1s and (i) P 2p fitting peaks of the OPBNP.

the insertion/extraction of more Na^+ and increases the storage capacity of Na^+. In addition, with the variety of doped atoms, the (002) diffraction peak of OPBNP became wider, reflecting the amorphization of porous carbon and the increased porosity of the material. The generation of pores is expected to enhance ion adsorption, making it easier to embed sodium on the carbon surface, thereby effectively improving the capacity and rate performance of the system.[39] The chemical composition and graphitic degree of the prepared materials were characterized by Raman spectroscopy. All samples show two characteristic bands of D and G (Fig. 2b), representing the disordered graphitic carbon and ordered graphite structure. The D bands of OPC, OPB, OPNP and OPBNP are 1335, 1334, 1329 and 1327 cm^{-1}, respectively, and the G bands are 1598, 1591, 1585 and 1580 cm^{-1}, respectively. The shift of the G band indicates that B, N and P are doped into the OP-derived carbon lattice.[32] The I_D/I_G ratios of OPC, OPB, OPNP and OPBNP are 0.84, 0.87, 0.93 and 0.99, respectively. A higher I_D/I_G value indicates a lower graphitization structure and higher defectivity. These defects are beneficial for the storage of sodium ions, thereby increasing the specific capacity of the material.[29]

The SSA and pore structure of the material can be obtained by the N_2 adsorption–desorption test, which is particularly important for electrochemical performance. The isothermal curves of OPC, OPB, OPNP, and OPBNP exhibit a combined IUPAC-type I and IV curve with a H_3 hysteresis loop in the relative pressure range of 0.4–1.0 (Fig. 2c and S2†), indicating the co-existence of micropore and mesopores.[40] The undoped and activated OPC exhibits a typical type IV structure, further confirming the changes in the pore structure after doping. Table 1 clearly shows the textural property parameters of OPC, OPB, OPNP and OPBNP. The OPC material just shows significantly low SSA (10.9 $m^2\ g^{-1}$), while the SSA of OPB, OPNP and OPBNP samples after hydrothermal doping and activation are enhanced to 871.9, 1894.9 and 1774.8 $m^2\ g^{-1}$, respectively. It is worth noting that the SSA of OPBNP is slightly smaller than that of OPNP, which may be due to the filling of certain pore structures by B doping, further indicating the successful doping of B. The pore size distribution of the four groups of samples is shown in Fig. 2d, S2a, S2b, inset and S2d.† It can be observed that all four materials exhibit a pore structure dominated by micropores and supplemented by mesopores. The number of micropores reaches a relative maximum at around 0.45, 0.5, and 1.29 for OPNP, OPBNP and OPB, respectively, and OPBNP shows the highest dV/dD value, indicating the most abundant microporous structure. For the supercapacitor electrode, the microporous structure is the main energy storage site, and the relatively large specific surface area also favors the full contact of the electrode active substance and the electrolyte, improving the energy storage capacity of supercapacitor electrode materials.[15,41] In comparison, OPC micropores have a more dispersed pore size distribution and a relatively high number of mesopores. The total pore volume of the OPBNP is 0.81 $cm^3\ g^{-1}$, and the average pore size is 1.82 nm, indicating that its pore structure is richer than OPC, OPB and OPNP (Table 1), which is consistent with SEM and TEM tests. These results show that the doping combined with the activation process can significantly change its specific surface area, pore volume and pore size distribution. It is well known that micropores can accommodate charges in the electrical double layer and provide more electrochemical reaction active sites for ion storage, while mesopores can provide fast ion diffusion paths, further boosting the rate performance of the electrodes.[12,21] Therefore, these hierarchical porous carbon materials doped with heteroatoms have great potential as electrode materials in SCs and SIBs.

The surface element chemical composition of OPBNP was carried out by XPS. As shown in Fig. 2e, the full XPS of OPBNP shows three distinct characteristic peaks of C 1s (285.05 eV), N 1s (400.04 eV), O 1s (532.29 eV) and two weak characteristic peaks of B 1s (184.22 eV) and P 2p (131.04 eV) (Fig. 2e inset), confirming the coexistence of C, O, N, B and P elements, respectively. The corresponding elemental contents were 84.21%, 11.46%, 3.28%, 0.90% and 0.15%, respectively. The high-resolution spectra of C 1s (Fig. S3†), N 1s, O 1s, B 1s and P 2p (Fig. 2f–i) further prove the existence of C, B, N, P and O elements to understand the chemical bonds formed on the surface of OPBNP. The C 1s spectrum shows obvious characteristic peaks at the binding energies of 284.75, 286.05, 287.61 and 288.91 eV, corresponding to C–C/sp^{2}C, C–B/C–P/sp^{2}C–N, C=O and C–O functional groups, respectively (Fig. S3†).[12,42] The N 1s spectrum contains three peaks with binding energies of 398.49, 400.32 and 401.9 eV, respectively (Fig. 3f). The corresponding valence structures include pyridine N (N-6)/N–B, pyrrole N (N-5) and graphite N/N=P.[41,43] N-6 and N-5 mainly act as the electron donor, generate defects to increase the active sites and provide pseudocapacitance contribution,[44] while graphitic N can increase the conductivity of the material.[45] For the O 1s spectrum (Fig. 2g), the characteristic peaks at 532.57, 533.87 and 535.2 eV can be attributed to C–O–C/C–O–H, O–B and –COOH functional groups, respectively.[41] The three characteristic peaks of B 1s are shown in Fig. 2h, and the corresponding functional groups are B–C (189.84 eV), B–N (190.97

Table 1 Textural properties of OPC, OPB, OPNP and OPBNP

Sample	d_{002} (nm)	I_D/I_G	$S_{BET}{}^a$ ($m^2\ g^{-1}$)	$V_{Total}{}^b$ ($cm^3\ g^{-1}$)	$V_{Micro}{}^c$ ($cm^3\ g^{-1}$)	$D_{aver}{}^d$ (nm)
OPC	0.374	0.84	10.9	0.053	0.003	19.54
OPB	0.378	0.87	871.9	0.36	0.28	1.64
OPNP	0.384	0.93	1894.9	0.83	0.75	1.75
OPBNP	0.392	0.99	1774.8	0.81	0.69	1.82

[a] BET surface area. [b] Total pore volume. [c] Micropore volume, calculated by applying Horvath–Kawazoe (HK) method, calculated by applying HK method. [d] Average pore diameter.

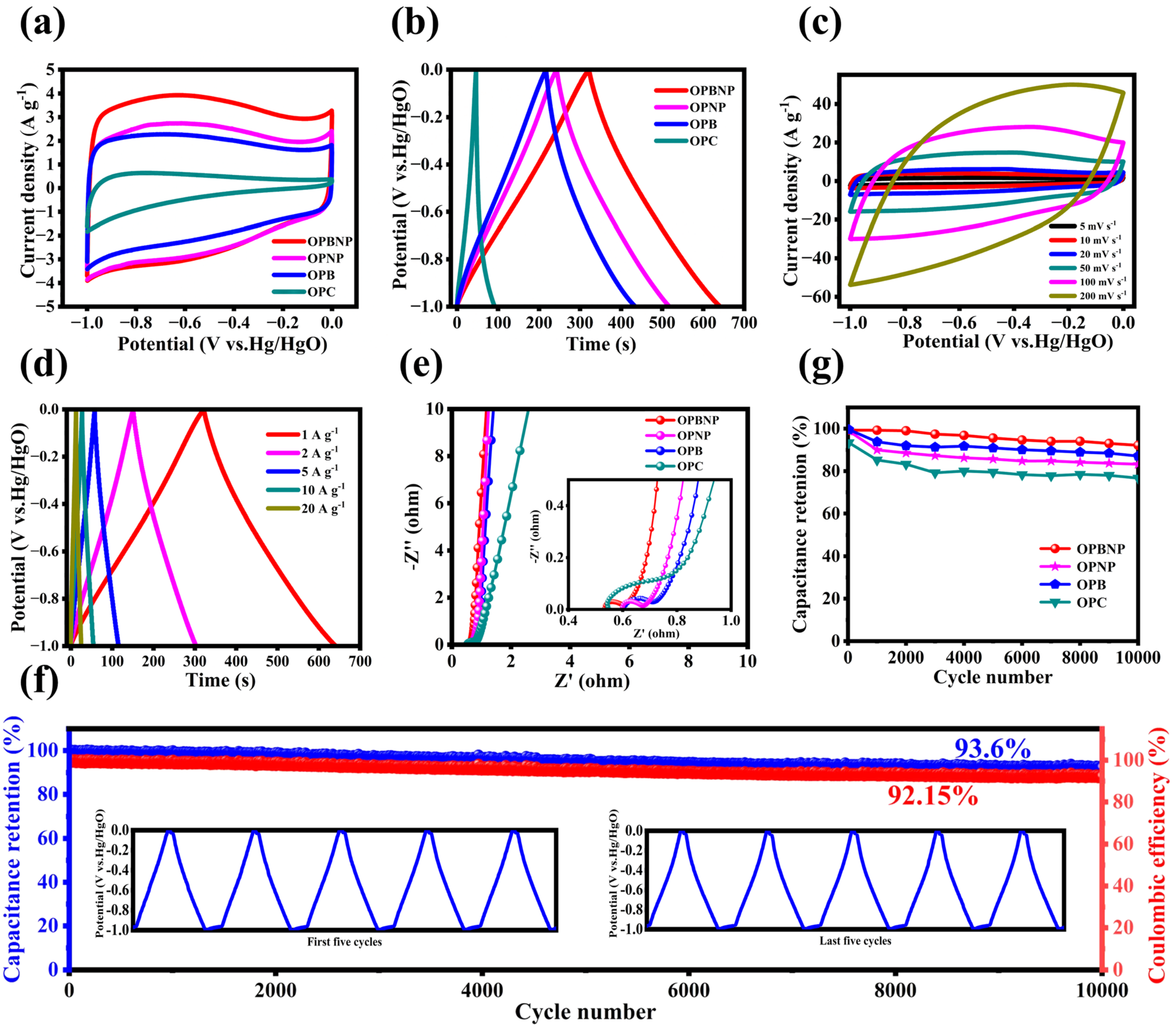

Fig. 3 Electrochemical performance of OPC, OPB, OPNP and OPBNP for supercapacitor in three-electrode system in 6 M KOH. (a) CV curves at 10 mV s^{-1}; (b) GCD curve at 1 A g^{-1}; (c) CV and (d) GCD curves of OPBNP at different scan rates and current densities; (e) EIS spectroscopy (inset: equivalent circuit diagram); (f) cycling performances at 5 A g^{-1} of OBNP (inset: GCD curves of the first and last five cycles); and (g) comparison chart of cycling performance of four samples.

eV) and B–O (191.82 eV); the P 2p spectrum has three characteristic peaks (Fig. 2i) with binding energies of 131.79 eV P–O group, 133.43 eV C–PO_3/C_2–PO_2 group and 134.66 eV P–C group, respectively.[42,46] The doping of heteroatoms can significantly improve the properties of porous carbon materials in terms of increasing conductivity and modulating disorder and defects of materials, thus promoting the formation of surface pseudocapacitance, which benefits the application of samples in the field of electrochemistry.[5,47,48]

3.2 Electrochemical properties

The electrochemical performances of the OPC, OPB, OPNP and OPBNP samples for the supercapacitor are presented in Fig. 3. As shown in Fig. 3a, the CV curve of OPC has the smallest area of CV at high voltage, which is a typical CV curve without any modification. Due to the low SSA, the contact between the electrolyte and the electrode material is limited, and the active sites of energy storage are few. The other three CV curves showed a quasi-rectangular shape at 10 mV s^{-1}, indicating the dominant double layer capacitor behavior.[49] The obvious hump on the rectangular CV curve intimates the partly pseudocapacitance due to the reversible redox reactions produced by heteroatoms.[47] It is noteworthy that the OPBNP shows the largest closed area due to its rich and uniform pore structure and ternary atom co-doping active sites, indicating its best capacitance performances. Fig. 3b shows that all the GCD curves present a nearly isosceles triangle shape at 1 A g^{-1}, illustrating the ideal electric double layer capacitance (EDLC) behaviors, which significantly agree with the CV results. It can also be observed that the discharge time of the samples (OPB, OPNP, OPBNP) is much longer than that of OPC, which may be attributed to the increase in the pseudocapacitance induced by heteroatoms and the increase in the SSA caused by the activation pore-forming. Furthermore, the specific capacitance of the OPBNP (318.8 F g^{-1}) is much higher than those of OPC (45.5 F g^{-1}), OPB (217.3 F g^{-1}) and OPNP (274.5 F g^{-1}), indicating that ternary doping can provide higher pseudocapacitance and more active sites for EDLC. As the scanning rate increases from 5 mV s^{-1} to 200 mV s^{-1}, the rectangular shape of the CV curve shifts slightly (Fig. 3c), indicating that the OPBNP electrode materials have low internal contact resistance, easy ion transport, and excellent rate performance. Fig. 3d displays the GCD curve of the OPBNP electrode at different current densities ranging from 1 to 20 A g^{-1}. The corresponding specific capacitance of OPBNP is 318.8, 303.6, 289.0, 271.0 and 248.0 F g^{-1} at 1, 2, 5, 10 and 20 A g^{-1}, respectively. It is easily observed that as the current density increases, the specific capacitance of the material also decreases. The specific capacitance of all the electrodes at different current densities is displayed in Fig. S4 and Table S1.† Clearly, the OPBNP electrodes show the highest specific capacitance at different current densities and exhibit the best capacitance retention of 77.8%. This excellent rate capability may be due to a synergistic effect between the doping of B/N/P elements, which increases the active site, and the rich pore structure, which can provide more ion channels, allowing the rapid transport of electrolyte ions to reach the electrode/electrolyte interface to complete charge storage.[50,51]

The EIS was carried out to explore the capability of electron/ion transport for the electrodes. As shown in Fig. 3e, all the curves exhibit a nearly straight line in the low-frequency region and a small semicircle arc in the high-frequency region. The intercept at the real axis indicates the inner resistance (R_s) generated by the contact effect within the electrode material, electrolyte ion resistance, and contact resistance of the active material/current collector, active material and the electrolyte.[47] The diameter of the semicircle arc on the real axis expresses the charge transfer resistance (R_{ct}) produced at the interface between the electrode and electrolyte. Based on the fitting results (the equivalent circuit diagram and fitting data are shown in Fig. S5 and Table S1†), the OPBNP electrode displays the lowest R_s and R_{ct} values of 0.54 Ω and 0.043 Ω, respectively, indicating low electron and charge transportation resistance.[52] In contrast to the OPBNP electrode, the other three electrodes show slight increases in R_s and R_{ct} values with the OPC of 0.55 Ω/0.092 Ω, OPB of 0.61 Ω/0.062 Ω, and OPNP of 0.60 Ω/0.053 Ω. The straight line corresponds to the Warburg impedance, in which the OPBNP electrode is almost vertical, demonstrating fast ionic diffusion in the porous electrode material. Therefore, the analysis results indicate that the ternary doping of B, N and P significantly reduces the charge transfer resistance and ion diffusion resistance due to the large SSA, rich hierarchical pores and a certain degree of graphitization, indicating the superior electrochemistry performance. Fig. 3f shows the long cycling performance of the four samples at 5 A g^{-1}. After 10 000 cycles, the OPBNP exhibits the most excellent cycle stability with a capacitance retention of 93.6% among the four samples, while OPB is 88.8%, OPNP is 83.5% and OPC is only 76.7%. The ultra-high capacitance retention of OPBNP far exceeds those of the other electrodes. This could be ascribed to the rich pore structure together with ternary element doping, which provides a more favorable channel for ion transport and gives abundant reaction active sites for complete charge storage. Besides, our B/N/P co-doped porous carbon shows obvious advantages compared with other biomass-derived heteroatom-doped biomass carbon reported previously (Table S2†). Therefore, these results indicate that OPBNP materials with a well-developed pore structure and heteroatom doping are ideal carbon-based electrode materials for high-performance supercapacitors.

To evaluate the capacitance performance of the obtained OPBNP samples in practical applications, a coin-type two-electrode symmetric supercapacitor was further assembled in 6 M KOH. As shown in Fig. 4a, the CV curves of the OPBNP//OPBNP tested from 5 to 200 mV s^{-1} exhibited quasi-rectangular shapes that are similar to those of the OPBNP electrode, indicating ideal capacitance characteristics and good rate performances. All GCD curves of OPBNP//OPBNP device exhibit the standard symmetrical triangle shapes ranging from 1 to 20 A g^{-1}, indicating good kinetic reversibility and excellent coulombic efficiency (Fig. 4b). As shown in Fig. S6,† as the current density increases, the specific capacitance decreases slowly. Based on eqn S3,† at 1 A g^{-1}, the capacitance of a single electrode can reach an impressive 257.2 F g^{-1} (with an electrode capacitance of 64.3 F g^{-1}). Remarkably, even at a high current density of 20 A g^{-1}, it can still maintain a significant capacitance of 224 F g^{-1}, representing 87.1% of the initial specific capacitance. Besides, it is worth mentioning that the OPBNP sample in this work shows superior capacitance than that of commercial AC (37.5 F g^{-1}),[53] indicating the huge practical potential of OPBNP as an energy storage device for supercapacitors.

Fig. 4c displays the energy density/power density relationship curve of the OPBNP//OPBNP symmetric supercapacitor. The energy density can reach 8.9 W h kg^{-1} at a power density of 499.7 W kg^{-1} and maintain 7.7 W h kg^{-1} at a higher power density (9996.4 W kg^{-1}) according to the formula in Text S1.† In addition, to further assess the practical applications of the OPBNP//OPBNP device, the assembled symmetrical button battery could be used to light up a commercial 1.5 V green light bulb (inset of Fig. 4c). Fig. 4d depicts the Nyquist curve of OPBNP//OPBNP. The impedance spectra show the lower resistance values of 0.1 Ω and 0.4 Ω for R_s and R_{ct}, respectively, indicating benign conductivity and fast charge transfer. Fig. 4e shows the long cycle performance of OPBNP//OPBNP battery at 5 A g^{-1}. It exhibits an excellent capacitance retention of 97.61% and a high coulombic efficiency of 98.24% after 10 000 cycles. This excellent cycle stability can be attributed to the synergistic effect of multiple atom doping (B, N and P) and the layered micropore and mesopore structures of OPBNP, which not only provide more active sites/defects for additional pseudo-capacitance but also enhance the permeability of the electrolyte to provide short and low-resistance ion diffusion channels for fast ion transport.

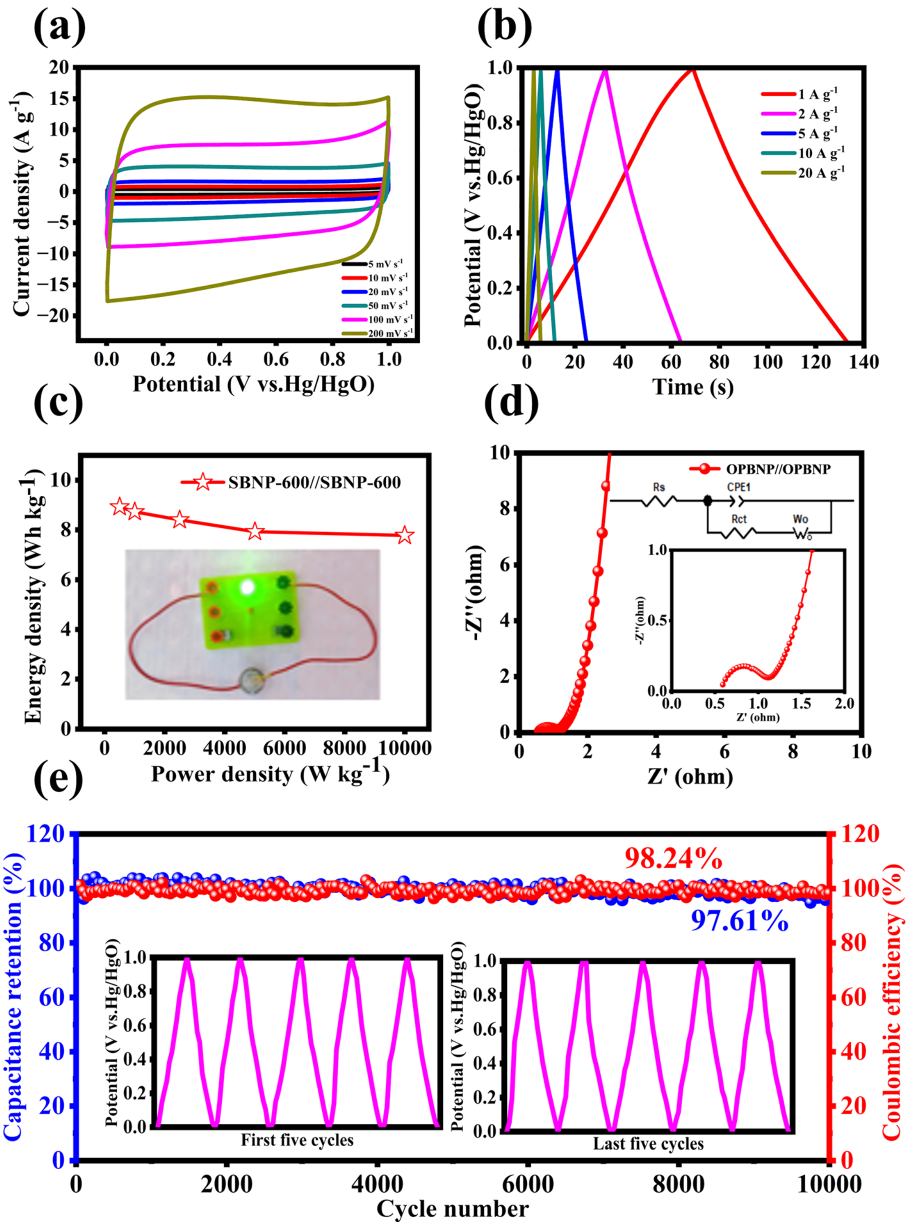

Fig. 4 Electrochemical properties of OPBNP//OPBNP coin-type symmetric supercapacitor in 6 M KOH electrolyte solution. (a) CV curves at different scan rates; (b) GCD curves at different current densities; (c) energy density and power density diagram of OPBNP//OPBNP, (inset): the design of energy storage device; (d) Nyquist diagram before cycling, inset: magnification view and equivalent circuit diagram in the middle and high-frequency region; and (e) long cycle performance at 5 A g^{-1}, (inset): GCD curves of the first and last five cycles.

The as-prepared OPBNP were also evaluated as anode materials for SIBs in half-cell with metal sodium foil as the counter electrode. As shown in Fig. 5a, in the first cycle, two apparent reduction peaks occur at 0.32 and 1.17 V for OPBNP electrodes, while the OPC electrode shows two reduction peaks at 0.19 and 1.06 V (Fig. S7a†). It is noteworthy that the deviation of the peak position can be attributed to the doping of multiple atoms and the activation process, thereby increasing the current response. The former peak for both samples may be related to the side reaction between the electrolyte and the surface groups, while the latter could be caused by the decomposition of the electrolyte and the formation of the SEI film at the interface. These reduction peaks are not observed in the subsequent 2nd, 3rd, and 4th cycles, indicating the irreversible reaction among the sodium ions and surface functional groups, which mainly occurs during the first charge–discharge process.[54] From the 2nd cycle, CV curves almost overlap with each other, suggesting the formation of the stable SEI layer that ensures benign reversibility and cycling stability.[26] Besides, an obvious reduction peak can be observed in the low potential region near 0.01 V, which is attributed to the embedding of Na^+ in the carbon layer to form NaC_X compounds.[55]

The constant current discharge–charge curves of OPC and OPBNP at 0.1 A g^{-1} were also studied, and the corresponding

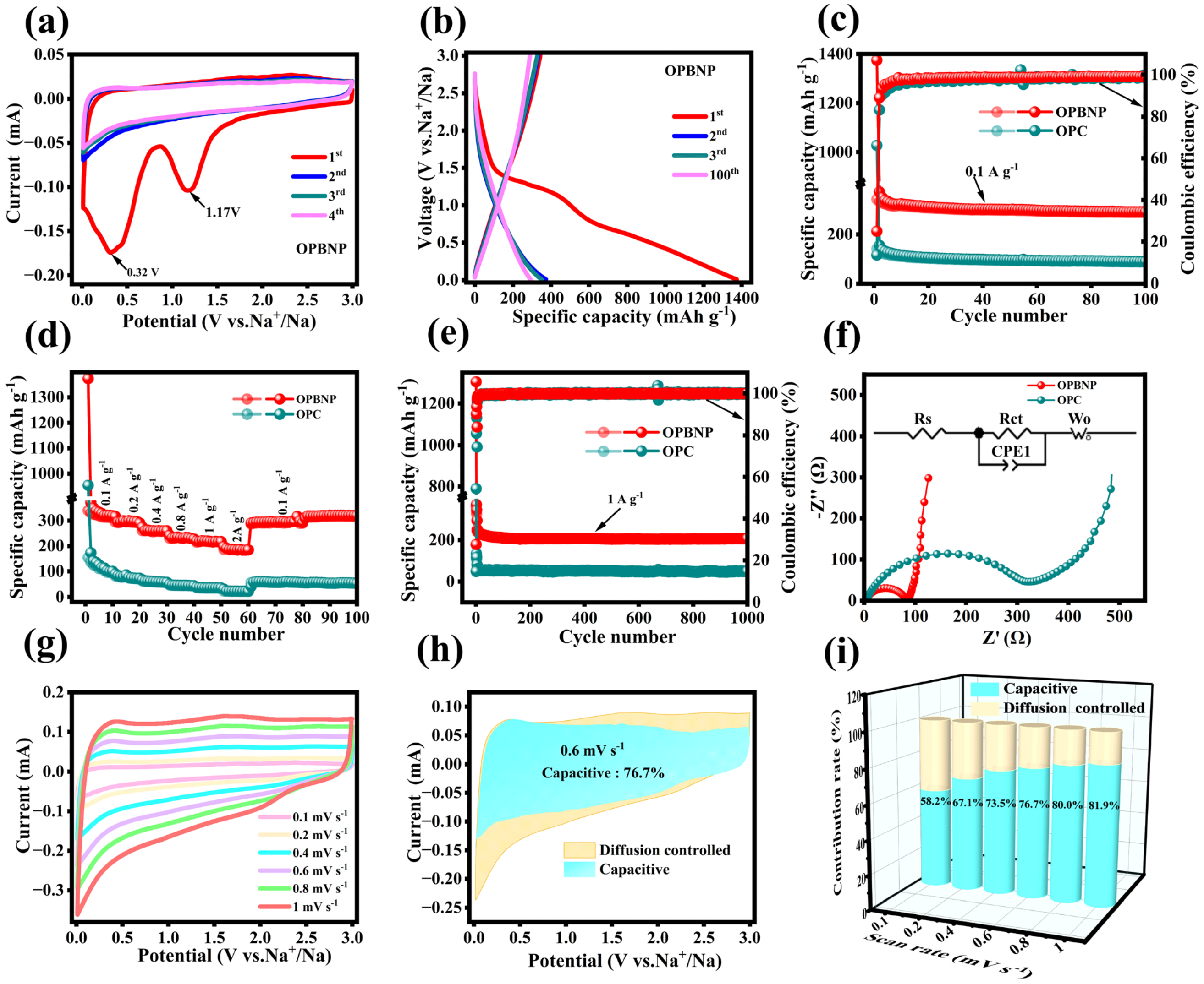

Fig. 5 Sodium storage performance of OPBNP material. (a) CV curves at 0.1 mV s^{-1}; (b) charge–discharge curves of 1st, 2nd, 3rd and 100th cycle at 0.1 A g^{-1}; (c) cycling performances at 0.1 A g^{-1}; (d) rate performances at different current densities; (e) cycling performances at 1 A g^{-1}; (f) EIS spectra and equivalent circuit diagrams before electrode cycling; (g) CV curves at different scan rates ranging from 0.1 to 1.0 mV s^{-1}; (h) capacitive and intercalated contributions at 0.6 mV s^{-1}; and (i) the ratio of capacitive contribution at the scan rates of 0.1, 0.2, 0.4, 0.6, 0.8 and 1.0 mV s^{-1}.

profiles of the 1st, 2nd, 3rd, and 100th cycles are shown in Fig. S7b† and 5b. As observed in the figures, both samples show clear plateaus in the first discharging process, corresponding to their respective peaks in the CV curves. In the first cycle, the OPBNP delivers an initial discharge/charge specific capacity of 1374.1/342.5 mA h g^{-1} with an initial coulombic efficiency of 25.0%, which is much higher than that of OPC (1027.3/141.0 mA h g^{-1}, 13.7%). This result indicates that heteroatom doping can improve the ICE of SIBs by increasing the graphite layer spacing, which is conducive to the insertion/extraction of sodium ions.[56] The low ICE could be ascribed to its large BET surface area, which significantly increases the formation of the SEI layer and associated side reactions at the electrode–electrolyte, resulting in large irreversible capacity loss.[57] Notably, it is very common that most biomass-derived porous carbons synthesized at lower carbonization temperature show large irreversible capacity loss in the first cycle, such as pomelo peel (1149.7/314.5 mA h g^{-1}, 27.3%),[58] seaweed (1342/287 mA h g^{-1}, 21.4%; 670/115 mA h g^{-1}, 17.2%; 639/186 mA h g^{-1}, 29.1%),[59] 3D carbon (902/221 mA h g^{-1}, 24.5%),[60] and carbon sphere (1249/303 mA h g^{-1}, 24.2%).[61] Besides, even though the ICE of OPBNP is low, its first charge capacity is still better than that obtained in previous studies. In addition, its reversible capacity after 1000 cycles has certain advantages. These results indicate the good sodium storage performance of the OPBNP electrodes. In the subsequent cycles, the discharge/charge specific capacities of the OPBNP at the 2nd, 3rd and 100th cycles are 373.5/333.0 mA h g^{-1}, 350.6/328.1 mA h g^{-1} and 292.3/289.8 mA h g^{-1} with the CE of 89.2%, 93.7% and 99.1%, respectively, verifying the good electrochemical reversibility. Fig. 5c shows the cycling performance of OPC and OPBNP at 0.1 A g^{-1}. It can be observed that the discharge specific capacity of OPBNP is still maintained at 292.3 mA h g^{-1} after 100 cycles with a capacity retention of 88.8%, which is much higher than that of OPC with the specific capacity of 91.0 mA h g^{-1} and capacity retention of 71.2%. These excellent properties are ascribed to multiatom doping, which could increase the interlay spacing of hard carbon material and is beneficial for the insertion/extraction of sodium ions. In addition, adequate heteroatom doping could improve the active sites, resulting in improved electrochemical properties. The rate capabilities (Fig. 5d) of OPC and OPBNP were measured at current densities of 0.1, 0.2, 0.4, 0.8, 1, and 2 and finally returned to 0.1 A g^{-1} for continuous 100 cycles. The corresponding average discharge specific capacities of OPBNP are 437.9 mA h g^{-1}, 298.2 mA h g^{-1}, 261.8 mA h g^{-1}, 232.7 mA h g^{-1}, 218.3 mA h g^{-1}, and 186.9 mA h g^{-1} at the rates of 0.1, 0.2, 0.4, 0.8, 1, and 2 A g^{-1}, respectively. Even when the rate is back to 0.1 A g^{-1}, it can still switch back to 294.1 mA h g^{-1} and maintain excellent cycle stability without obvious degradation after 40 cycles. It can also be observed that the specific capacities of OPBNP at various current densities are significantly higher than those of OPC. This result is consistent with the former cycle performances shown in Fig. 5c, further confirming that heteroatom doping plays an important role in enhancing the sodium ion storage properties. Besides, the OPBNP showed extremely stable cycling performance even at a high current density of 1 A g^{-1} (activate the first three cycles at a low current density of 0.1 A). The discharge/charge specific capacity is maintained at 206.6/206.4 mA h g^{-1} after 1000 cycles with a capacity retention of 63.79% (Fig. 5e). In contrast, the discharge/charge capacity of OPC is only 48.5/48.0 mA h g^{-1}, indicating that heteroatom doping has a positive impact on enhancing the electrochemical performance of sodium-ion batteries. It is worth emphasising that the OPBNP electrode also shows a high-rate performance compared to other previous studies (Table S3†). The superior rate capability of the OPBNP electrode could be attributed to the micropore-dominated hierarchical pore structure, larger SAA and multi-atom doping. First, the micropore-dominated hierarchical pore structure interpenetrates with each other to form an interpenetrating network, which can promote electrolyte penetration and allow for rapid ion/electron conduction, thereby enhancing the ion dynamics in micropores. Second, the high surface area of the microporous carbon (1774.8 m^2 g^{-1}) offers abundant active sites for ion storage, increasing the capacity value of the battery. Besides, it can enhance electrode stability and buffer volume changes. Third, the B/N/P co-doping also helps to improve the electrical conductivity and reaction kinetics, resulting in improved rate performance.[62,63]

Furthermore, as shown in Fig. S8,† the SEM image indicates that the carbon nanosheets and interpenetrate network structures were well maintained after repeated Na$^+$ insertion/extraction for 1000 cycles. To further confirm the enhanced sodium storage performance of OPBNP, EIS was performed on OPC and OPBNP before cycling. As shown in Fig. 5f, both Nyquist plots display a semicircle in high-medium frequency related to the charge transfer resistance (R_{ct}), and a quasi-vertical line in low frequency corresponding to the relatively low Warburg impedance and fast ion diffusion rate. The corresponding R_s and R_{ct} of the OPBNP are 3.2 Ω and 72.4 Ω, respectively, which are significantly lower than those of the OPC electrode (4.1 Ω and 291.8 Ω), as shown in Table S4.† The excellent sodium storage performance of OPBNP is ascribed to the existence of highly interconnected pores and heteroatoms doping in the carbon lattice produced by hydrothermal doping and KOH activation, which contributes to the penetration of electrolytes and provides good conditions for Na$^+$ storage.[64] The above results show that B/N/P doping has an indispensable effect on the capacity storage of SIBs.

To further study the kinetic behavior of the OPBNP electrodes, the CV curves were tested at different rates of 0.1, 0.2, 0.4, 0.6, 0.8, and 1 mV s^{-1}. As shown in Fig. 5g, the CVs have a similar shape at different scan rates, but the cathodic peak current increases as the scanning rate increases. The slight increase in contrary shifts for the cathodic/anodic peaks implies the improved kinetics of the capacitive–controlled process. The proportion of capacitive behavior in the current response can be quantitatively evaluated using the following formula:[62]

$$i(V) = k_1 v + k_2 v^{1/2} \tag{1}$$

where i is the current and k_1 and k_2 are adjustable empirical constants. In the current response, the relationship between the capacitive behavior corresponding to $k_1 v$ and the diffusion control characteristics of $k_2 v^{1/2}$ obtains the corresponding slope (k_1) and intercept (k_2) at a certain voltage to calculate the current value contributed by the pseudo-capacitance behavior and diffusion behavior.[18] As illustrated in Fig. 5h, the calculated capacitive contribution ratio is 76.7% at a scan rate of 0.6 mV s^{-1}. With the increase in scanning rate, the capacitive contribution ratios increased from 58.2% to 81.9% with the scan rates ranging from 0.1 to 1.0 mV s^{-1}, indicating that the capacitive behavior governs the entire electrochemical behavior, which helps to enhance the performance of the OPBNP electrode at high current densities (Fig. 5i). These results suggest that the high contribution ratio due to the Na$^+$ adsorption of OPBNP is mainly caused by the porous structure and the active sites provided by heteroatom doping, thus further explaining its excellent electrochemical performance.

The above electrochemical test results indicate that OPBNP is suitable as a promising electrode for both supercapacitors and SIBs. The good electrochemical performance could be ascribed to the microstructural characteristics, and its electrochemical storage mechanism can be explained, as shown in Fig. 6. First, the interpenetrated porous carbon network, achieved by hydrothermal doping and KOH activation, boasts a notably high specific surface area. This characteristic enhances the contact interface between the electrolyte and electrode, offering an increased number of adsorption sites for charge accumulation. Additionally, the abundant pore structure, comprising both micropores and mesopores, facilitates efficient electron transfer and charge transport. This structure also reduces the ion diffusion time, thereby enhancing the performance of the material in multiple aspects. Moreover, the co-doping of polyheteroatoms serves to regulate defects and disorders within the porous carbon, which improves the conductivity and introduces additional pseudocapacitance through surface redox reactions. By combining these factors

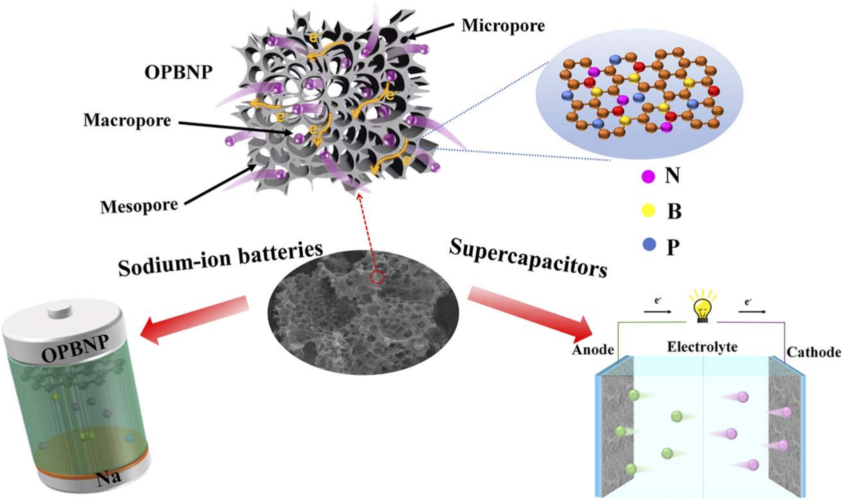

Fig. 6 Schematic illustration of the electrochemical storage mechanism for the OPBNP electrode.

and leveraging their synergistic effects, porous carbon derived from orange peel emerges as the preferred material for next-generation energy storage systems.

4. Conclusion

In summary, new B/N/P co-doped porous carbon (OPBNP) was successfully prepared by hydrothermal doping combined with KOH activation using low-cost orange peel as a raw material for the energy storage applications of SCs and SIBs. Structural characterization and chemical composition analysis showed that OPBNP material exhibited a high SSA, large interlayer spacing, rich micro/mesoporous structure, and enhanced disorder, which were favorable for the improvement of electrochemical performance. Benefiting from these structural features, when employed as supercapacitor electrodes, the OPBNP exhibited a high specific capacity of 289 F g^{-1} at 5 A g^{-1}, with only 6.4% capacitance loss after 10 000 cycles, and could still maintain 248.0 F g^{-1} at 20 A g^{-1}. Moreover, the assembled OPBNP//OPBNP symmetric supercapacitor exhibited an energy density of 8.9 W h kg^{-1} at a power density of 499.7 W kg^{-1}. As anodes for SIBs, the OPBNP electrode also showed outstanding rate capability and excellent long cycling life of 63.79% capacity retention after 1000 cycles. The method adopted in this paper achieves the scientific "transformation" of agricultural waste, promotes the development of energy storage devices, solves the problems caused by the irrational use of agricultural waste, and provides a new way for balancing the ecological environment.

Data availability

The data that support the findings of this study are available on request from the corresponding authors.

Author contributions

Y. C., H. Y. and H. T. designed the research. Y. L. synthesized and characterized the prepared materials. Y. L., X. Z. and S. L. performed the electrochemical performances. Y. L., X. Z. and S. L. co-wrote the paper with input from Y. C., H. Y., G. X. W. and H. T. for analysis of the data and preparation of this paper. The paper was revised by all authors.

Conflicts of interest

There are no conflicts to declare.

Acknowledgements

This work was financially supported by the Foundation from Jiangsu Province Industry-University-Research Collaboration (BY20231163, BY20231179), and the Modern Agricultural Projects of Zhenjiang (NY2019022).

References

1 S. Zhou, L. Zhou, Y. Zhang, J. Sun, J. Wen and Y. Yuan, *J. Mater. Chem. A*, 2019, **7**, 4217–4229.
2 A. Khedulkar, B. Pandit, V. Dang and R. Doong, *Sci. Total Environ.*, 2023, **869**, 161441.
3 M. Yan, Y. Qin, L. Wang, M. Song, D. Han, Q. Jin, S. Zhao, M. Zhao, Z. Li, X. Wang, L. Meng and X. Wang, *Nanomaterials*, 2022, **12**, 930.
4 Y. Bai, C. Zhang, F. Rong and Z. Guo, *Chem.–Eur. J.*, 2024, **30**, e20230415.
5 Y. Li, M. Chen, B. Liu, Y. Zhang, X. Liang and X. Xia, *Adv. Energy Mater.*, 2020, **10**, 2000927.
6 L. Luo, Y. Lan, Q. Zhang, J. Deng, L. Luo, Q. Zeng, H. Gao and W. Zhao, *J. Energy Storage*, 2022, **55**, 105839.
7 Z. Ma, A. Song, Z. Liu, Y. Guo, X. Yang, Q. Li, Y. Fan, L. Dai, H. Tian, X. Qin, H. Liu, G. Shao and G. Wang, *Adv. Funct. Mater.*, 2023, 2301112.
8 P. Ma, S. Yao, Z. Wang, F. Qi and X. Liu, *Sep. Purif. Technol.*, 2023, **311**, 123250.
9 H. Tian, J. Liang and J. Liu, *Adv. Mater.*, 2019, 1903886.

10 C. Zhao, Y. Ding, Y. Huang, N. Li, Y. Hu and C. Zhao, *Appl. Surf. Sci.*, 2021, **555**, 149726.

11 L. Li, M. Sun, Z. Xu, Z. Wang, K. Liu, Y. Chen, Z. Wang, H. Chen and H. Yang, *Colloids Surf., A*, 2023, **661**, 130927.

12 W. Chen, X. Wang, C. Liu, M. Luo, P. Yang and X. Zhou, *Waste Manage.*, 2020, **102**, 330–339.

13 R. Lu, D. Xu, H. Pan, C. Zhua, D. Wang, X. Meng, Y. Li, M. Imtiaz, S. Zhu and J. Ma, *J. Energy Storage*, 2019, **22**, 60–67.

14 K. Hong, L. Qie, R. Zeng, Z. Yi, W. Zhang, D. Wang, W. Yin, C. Wu, Q. Fan, W. Zhang and Y. Huang, *J. Mater. Chem. A*, 2014, **2**, 12733–12738.

15 C. Liu, W. Chen, S. Hong, M. Pan, M. Jiang, Q. Wu and C. Mei, *Nanomaterials*, 2019, **9**, 405.

16 J. Zhang, J. Duan, Y. Zhang, M. Chen, K. Ji and C. Wang, *Chem.–Eur. J.*, 2021, **8**, 3544–3552.

17 Q. Jin, K. Wang, P. Feng, Z. Zhang, S. Cheng and K. Jiang, *Energy Storage Mater.*, 2020, **27**, 43–50.

18 G. Zhao, D. Yu, C. Chen, L. Sun, C. Yang, H. Zhang, B. Du, F. Sun, Y. Sun and M. Yu, *J. Electroanal. Chem.*, 2020, **878**, 114551.

19 L. Cong, G. Tian, D. Luo, X. Ren and X. Xiang, *J. Electroanal. Chem.*, 2020, **871**, 114249.

20 L. Cao, Y. Wang, H. Hu, J. Huang, L. Kou, Z. Xu and J. Li, *J. Mater. Sci.: Mater. Electron.*, 2019, **30**, 21323–21331.

21 M. Khan, N. Ahmad, K. Lu, Z. Sun, C. Wei, X. Zheng and R. Yang, *Solid State Ionics*, 2020, **346**, 115223.

22 X. Wang, L. Cao, R. Lewis, T. Hreid, Z. Zhang and H. Wang, *Renew. Energy*, 2020, **162**, 2306–2317.

23 J. Yu, X. Li, Z. Cui, D. Chen, X. Pang, Q. Zhang, F. Shao, H. Dong, L. Yu and L. Dong, *Renew. Energy*, 2021, **163**, 375–385.

24 K. Wang, Z. Zhang, Q. Sun, P. Wang and Y. Li, *J. Mater. Sci.*, 2020, **55**, 10142–10154.

25 L. Tang, Y. Zhou, X. Zhou, Y. Chai, Q. Zheng and D. Lin, *J. Mater. Sci.: Mater. Electron.*, 2019, **30**, 2600–2609.

26 S. Tao, W. Xu, J. Zheng, F. Kong, P. Cui, D. Wu, B. Qian, S. Chen and L. Song, *Carbon*, 2021, **178**, 233–242.

27 R. Muruganantham, F. Wang and W. Liu, *Electrochim. Acta*, 2022, **424**, 140573.

28 A. R. Kannan, M. Kannan and G. Nataraj, *Renewable Energy*, 2020, **146**, 1781–1795.

29 N. Shaji, C. Ho, M. Nanthagopal, P. Santhoshkumar, G. Sim and C. Lee, *J. Alloys Compd.*, 2021, **872**, 159670.

30 J. Ryu, M. Park and J. Cho, *J. Electrochem. Soc.*, 2015, **163**, A5144.

31 Q. Sun, Z. Wu, B. Cao, X. Chen, C. Zhang, T. Shaymurat, H. Duan, J. Zhang and M. Zhang, *Appl. Surf. Sci.*, 2022, **592**, 153254.

32 S. Muduli, V. Naresh and S. Martha, *J. Electrochem. Soc.*, 2020, **167**, 090512.

33 J. Xiang, W. Lv, C. Mu, J. Zhao and B. Wang, *J. Alloys Compd.*, 2017, **701**, 870–874.

34 K. Zhao, C. Chen, M. La and C. Yang, *Micromachines*, 2022, **13**, 806.

35 X. Liu, H. Wang, Y. Cui, X. Xu, H. Zhang, G. Lu, J. Shi, W. Liu, S. Chen and X. Wang, *J. Mater. Sci.*, 2018, **53**, 6763–6773.

36 H. Wan, X. Shen, H. Jiang, C. Zhang, K. Jiang, T. Chen, L. Shi, L. Dong, C. He, Y. Xu, J. Li and Y. Chen, *Energy*, 2021, **231**, 121102.

37 L. Pei, H. Cao, L. Yang, P. Liu, M. Zhao, B. Xu and J. Guo, *Ionics*, 2020, **26**, 5535–5542.

38 X. Zhang, R. Huang, F. Wu, R. Chen and L. Li, *Nano Energy*, 2023, **117**, 108913.

39 A. Saha, T. Sharabani, E. Evenstein, G. Nessim, M. Noked and R. Sharma, *J. Electrochem. Soc.*, 2020, **167**, 090505.

40 N. Kim, Y. Yun, M. Song, S. Hong, M. Kang, C. Leal, Y. Park and H. Jin, *ACS Appl. Mater. Interfaces*, 2016, **8**, 3175–3181.

41 X. Fu, J. Chang, W. Guo, T. Gu, Y. Liu, L. Chen, G. Wang and F. Bao, *J. Power Sources*, 2024, **603**, 234474.

42 Y. Ma, X. Zhang, Z. Liang, C. Wang, Y. Sui, B. Zheng, Y. Ye, W. Ma, Q. Zhao and C. Qin, *Electrochim. Acta*, 2020, **337**, 135800.

43 J. Peng, X. Dai, J. Huang, J. Zeng, L. Zheng and H. Chen, *J. Energy Storage*, 2023, **59**, 106498.

44 J. Qu, C. Geng, S. Lv, G. Shao, S. Ma and M. Wu, *Electrochim. Acta*, 2015, **176**, 982–988.

45 X. Jiang, J. Zhou, H. Liu, Y. Chen and C. Lu, *Colloids Surf., A*, 2022, **650**, 129605.

46 G. Chen, Z. Hu, H. Su, J. Zhang and D. Wang, *Colloids Surf., A*, 2023, **656**, 130528.

47 X. Yue, H. Yang, P. An, Z. Gao, H. Li and F. Ye, *Dalton Trans.*, 2022, **51**, 12125–12136.

48 G. Zhao, Y. Li, G. Zhu, J. Shi, T. Lu and L. Pan, *ACS Sustain. Chem. Eng.*, 2019, **7**, 12052–12060.

49 Y. Chao, S. Chen, Y. Xiao, X. Hu, Y. Lu, H. Chen, S. Xin and Y. Bai, *J. Energy Storage*, 2021, **35**, 102331.

50 C. Liu, W. Chen, M. Li, S. Hong, W. Li, M. Pan, Q. Wu and C. Mei, *RSC Adv.*, 2019, **9**, 19441.

51 M. Lu, W. Yu, J. Shi, W. Liu, S. Chen, X. Wang and H. Wang, *Electrochim. Acta*, 2017, **251**, 396–406.

52 X. Su, J. Chen, G. Zheng, J. Yang, X. Guan, P. Liu and X. Zheng, *Appl. Surf. Sci.*, 2018, **436**, 327–336.

53 B. Yang, D. Zhang, J. He, Y. Wang, K. Wang, H. Li, Y. Wang, L. Miao, R. Ren and M. Xie, *Carbon Lett.*, 2020, **30**, 709–719.

54 X. Xue, Y. Weng, Z. Jiang, S. Yang, Y. Wu, S. Meng, C. Zhang, Q. Sun and Y. Zhang, *J. Anal. Appl. Pyrolysis*, 2021, **157**, 105215.

55 J. Wang, Y. Li, P. Liu, F. Wang, Q. Yao, Y. Zou, H. Zhou, M. Balogun and J. Deng, *J. Cent. S. Univ.*, 2021, **28**, 361–369.

56 Q. Jin, W. Li, K. Wang, H. Li, P. Feng, Z. Zhang, W. Wang and K. Jiang, *Adv. Funct. Mater.*, 2020, **30**, 1909907.

57 H. Zhang, Z. Yang, K. Qiao, G. Jia, H. Sai, Y. YLiu, W. He and J. Cui, *Colloids Surf., A*, 2022, **648**, 129400.

58 K. Hong, L. Qie, R. Zeng, Z. Yi, W. Zhang, D. Wang, W. Yin, C. Wu, Q. Fan, W. Zhang and Y. Huang, *J. Mater. Chem. A*, 2014, **2**, 12733–12738.

59 C. Senthil, J. Park, N. Shaji, G. Sim and C. Lee, *J. Energy Chem.*, 2022, **64**, 286–295.

60 P. Wang, B. Yang, G. Zhang, L. Zhang, H. Jiao, J. Chen and X. Yan, *Chem. Eng. J.*, 2018, **353**, 453–459.

61 Y. Qu, Z. Zhang, K. Du, W. Chen, Y. Lai, Y. Liu and J. Li, *Carbon*, 2016, **105**, 103–112.

62 B. Yin, S. Liang, D. Yu, B. Cheng, I. Egun, J. Lin, X. Xie, H. Shao, H. He and A. Pan, *Adv. Mater.*, 2021, **33**, 2100808.

63 W. Chen, M. Wan, Q. Liu, X. Xiong, F. Yu and Y. Huang, *Small Methods*, 2019, **3**, 1800323.

64 N. Sun, J. Qiu and B. Xu, *Adv. Energy Mater.*, 2022, **12**, 2200715.